



# LaCeO<sub>x</sub> coupled N-doped graphene/Ru single-atoms as a binary-site catalyst for efficient hydrogen evolution based on hydrogen spillover

Vandung Dao<sup>a,b,1</sup>, Hyuk Choi<sup>c,1</sup>, Sunny Yadav<sup>a</sup>, Juan D. Jiménez<sup>b</sup>, Chiyeop Kim<sup>a</sup>, Tuan Van Nguyen<sup>a</sup>, Kai Chen<sup>a</sup>, Periyayya Uthirakumar<sup>a</sup>, Quyet Van Le<sup>a</sup>, Sanjaya D. Senanayake<sup>b</sup>, Hyun You Kim<sup>c,\*</sup>, In-Hwan Lee<sup>a,\*</sup>

<sup>a</sup> Department of Materials Science and Engineering, Korea University, Seoul 02841, Republic of Korea

<sup>b</sup> Chemistry Division, Brookhaven National Laboratory, Upton, NY, USA

<sup>c</sup> Department of Materials Science and Engineering, Chungnam National University, Daejeon 34134, Republic of Korea

## ARTICLE INFO

### Keywords:

Hydrogen evolution reaction  
LaCeO<sub>x</sub>  
N-doped graphene  
Ruthenium  
Single-atoms

## ABSTRACT

Based on the hydrogen spillover effect, versatile binary-site catalysts are promising for the alkaline hydrogen evolution reaction (HER). In which one site can adsorb and dissociate water, while the neighboring site is favorable for liberating hydrogen. Inspired by these possibilities, oxygen vacancy (O<sub>v</sub>)-rich LaCeO<sub>x</sub> coupled N-doped graphene/Ru single-atoms (LaCeO<sub>x</sub>@NGr/Ru<sub>1</sub>) was synthesized as an efficient dual-site HER catalyst. It delivered an impressive low overpotential of 22 mV at a current density of 10 mA cm<sup>-2</sup> and a slight Tafel slope of 40 mV dec<sup>-1</sup> in an alkaline medium, outstanding the advanced Ru-based catalysts. Moreover, this promising binary-component catalyst exhibited higher mass activity and longer lasting durability than commercial Pt/C catalyst (20 wt%). Experimental and theoretical investigations provided insights into the HER mechanisms of LaCeO<sub>x</sub>@NGr/Ru<sub>1</sub> based on three indispensable steps: water adsorption and dissociation on O<sub>v</sub>-rich LaCeO<sub>x</sub>, diffusion of generated H<sup>\*</sup> species towards Ce<sup>3+</sup>-N-Ru<sub>1</sub> bridges, and hydrogen evolution on Ru<sub>1</sub> sites.

## 1. Introduction

Hydrogen (H<sub>2</sub>) as a clean and scalable energy source holds great promise to enable sustainability and overcome global warming issues caused by traditional fossil fuels [1–3]. Compared to conventional approaches, e.g., steam reforming of natural gas, electrochemical water splitting electrified by renewable sources is a promising way of producing hydrogen with zero emissions [4]. An ideal hydrogen evolution reaction (HER) electrocatalyst should converge three merits: high activity, durability, and low cost [5]. In this regard, Pt-based catalysts are currently recognized as the benchmark because of their low binding energy to hydrogen, resulting in low overpotentials and fast kinetics for HER [6]. However, Pt-based materials still have intrinsic weaknesses, including high cost and poor durability, limiting their HER practical applications. Thus, exploring better alternatives to replace Pt-based materials is highly desirable. In an alkaline medium, an HER process involves two electrochemical reaction steps [7]. First, water is adsorbed and dissociated to produce adsorbed hydrogen (H<sub>2</sub>O → HO\* + H\*)

(Volmer step). Then, the combination of generated H\* into molecular H<sub>2</sub> occurs (H\* + H\* → H<sub>2</sub>; Heyrovsky or Tafel step) [8]. One promising possibility to improve the metallic catalytic property is to use binary-site systems, where defect-rich oxides will be coupled with single-atom-supported carbon-based materials, thus delivering excellent HER performance based on the hydrogen spillover effect [9–11].

Cerium oxide (ceria: CeO<sub>2</sub>) and its modified derivatives are versatile materials in many advanced important processes such as catalysis, energy conversion, environmental, magnetics, sensing, and biomedical applications [12–14], which is generally governed by its capacity to produce oxygen vacancies (O<sub>v</sub>) due to the easily convertible valence states of cerium ions (Ce<sup>3+</sup>–4 f<sup>1</sup> and Ce<sup>4+</sup>–4 f<sup>0</sup>) [15–17]. In particular, the interaction between water and ceria has drawn remarkable attention experimentally and theoretically [18]. In this regard, the (111) facet has been mainly focused on since it is the most stable surface [19]. H<sub>2</sub>O molecules are adsorbed on both sites: Ce<sup>4+</sup> ions and O<sub>v</sub> with neighboring Ce<sup>3+</sup> ions [20]. The coexistence of active Ce<sup>3+</sup> species subsequently helps to dissociate water [21]. Since introducing the trivalent cations to

\* Corresponding authors.

E-mail addresses: [kimhy@cnu.ac.kr](mailto:kimhy@cnu.ac.kr) (H.Y. Kim), [ihlee@korea.ac.kr](mailto:ihlee@korea.ac.kr) (I.-H. Lee).

<sup>1</sup> These authors have contributed equally to this work and should be considered co-first authors

ceria, the oxygen vacancy is created to satisfy the missing positive charge and improve the oxygen storage ability of a typical metal/CeO<sub>2</sub> system [22]. For instance, two La<sup>3+</sup> ions substitute for Ce<sup>4+</sup> ions, one O<sub>v</sub> is required to balance the charge, and forming two Ce<sup>3+</sup> ions simultaneously in ceria [13,23–25]. Therefore, the as-generated La-doped ceria (LaCeO<sub>x</sub>) will likely be active for water adsorption and dissociation. On the other hand, surface hybridization with graphene-based materials can further improve the catalytic properties of ceria-based materials [26].

Among carbonaceous supports, graphene (Gr) and its doped derivatives, being thick atomic sheets with a two-dimensional sp<sup>2</sup>-hybridized carbon structure, have attracted much attention because they have large surface area, excellent electrical conductivity and electrochemical properties, and chemical stability [27–29]. As the best evidence, nitrogen-doped graphene (NGr) is a promising catalyst support due to its unique electronic properties resulting from three types of nitrogen-carbon bonds: pyridinic N, pyrrolic N, and quaternary N [30–32]. In fact, each N atom donates an excess electron which is delocalized over the whole network, while the as-obtained NGr preserves its flat structure and excellent conductivity [33]. On the other hand, the presence of electron-rich nitrogen sites in the N-containing carbonaceous supports is advantageous for anchoring other metallic catalysts, e.g., single Ru atoms [34–36]. Single atoms (SAs) possess superior catalytic activity compared to nanoparticle and nanocluster forms [37]. They are also perfectly dispersed on a support material [38]. Further, the SAs regularly provide a well-defined coordination environment to the catalytic reactions, benefiting from improving atomic utilization. Ruthenium (Ru) is an excellent candidate to replace commercial Pt/C catalysts in an alkaline HER because it has a low cost, and its hydrogen adsorption strength is similar to the Pt-based catalysts [39–42]. In addition, Ru SAs, not nanoparticles or nanoclusters, anchored on heteroatom-doped carbon have exhibited an appropriate adsorption strength of H\* species, resulting in improved HER performance [43]. For example, Li et al. reported on Ru/N-C as an effective HER catalyst in an alkaline medium [44], while Kweon et al. claimed the Ru/C is very active for hydrogen evolution in both acid and alkaline electrolytes [45].

This work proposed a practical approach to produce an efficient dual-site HER catalyst: defect-rich LaCeO<sub>x</sub> combined N-doped graphene/Ru single-atoms (LaCeO<sub>x</sub> @NGr/Ru<sub>1</sub>). The as-obtained dual-site material exhibited an impressive HER performance in an alkaline medium, outperforming the currently reported Ru-based catalysts. It further delivered higher mass activity and long-lasting durability than the state-of-the-art Pt/C catalysts. In addition, the catalytic superiority of the LaCeO<sub>x</sub> @NGr/Ru<sub>1</sub> catalyst was theoretically studied by density functional theory (DFT) calculations based on knowledge of the structural, electronic, and catalytic properties of each component: LaCeO<sub>x</sub>, NGr, and Ru single atoms. In this picture, water adsorption and dissociation were performed on O<sub>v</sub>-rich LaCeO<sub>x</sub>, Ce<sup>3+</sup>-N-Ru<sub>1</sub> bridges speed of the diffusion of generated H\* species, and finally Ru<sub>1</sub> sites host the hydrogen evolution. Accordingly, experimental and theoretical studies provided clear insights into the mechanism of LaCeO<sub>x</sub> @NGr/Ru<sub>1</sub> towards an alkaline HER. They shed new light on fabricating a versatile three-component dual-site catalyst for efficient and long-lasting hydrogen production reactions.

## 2. Experimental section

### 2.1. Fabrication of LaCeO<sub>x</sub>

La(NO<sub>3</sub>)<sub>3</sub>·6 H<sub>2</sub>O (0.15 g), Ce(NO<sub>3</sub>)<sub>3</sub>·6 H<sub>2</sub>O (1.5 g), and Na<sub>2</sub>CO<sub>3</sub> (4.3 g) were introduced in 45 mL of distilled water to fabricate ~10 wt% La-doped ceria. The solution was sonicated, stirred for 1 h, and transferred into a 50-mL Teflon-lined stainless-steel autoclave. The reaction temperature was increased to 180 °C with a heating rate of 2 °C min<sup>-1</sup> and maintained for 24 h in an electric oven. After that, the material was

collected by centrifugation at 10,000 rpm for 20 min. The product was washed with distilled water and dried at 80 °C in the air for 12 h. The final material, LaCeO<sub>x</sub>, was obtained by calcination at 500 °C in the air for 2 h. An undoped CeO<sub>2</sub> was also prepared using the same procedure but without introducing La salt.

### 2.2. Fabrication of LaCeO<sub>x</sub>@NGr/Ru<sub>1</sub>

200 mg of the as-synthesized LaCeO<sub>x</sub> powder was dispersed in 60 mL of distilled water containing 60 mg of glucose and 60 mg of dicyandiamide. Next, a suitable amount of Ru<sup>3+</sup> precursor (1 g RuCl<sub>3</sub>·3 H<sub>2</sub>O in 20 mL of water) was added to the above solution. The resulting solution was sonicated and stirred for 1 h at 25 °C to achieve a uniform suspension. The suspension was freeze-dried for 72 h until the water was wholly sublimated. The product was then pyrolyzed at 800 °C in argon for 3 h to obtain the LaCeO<sub>x</sub> @NGr/Ru<sub>1</sub> composite with a Ru loading of 1.5 wt%. Pure CeO<sub>2</sub> was the precursor to prepare the CeO<sub>2</sub> @NGr/Ru<sub>1</sub> composite with the same Ru loading. The Ru-free LaCeO<sub>x</sub> @NGr composite was also prepared without adding Ru salt.

### 2.3. Characterizations

The morphological observation of the as-prepared materials was performed using spherical aberration-corrected transmission electron microscopy (TEM; JEM-2010 microscope, JEOL). The crystallinity properties were investigated by X-ray diffraction instrument (XRD; D/Max 2005, Rigaku) with Cu-Kα radiation (λ = 1.54178 Å). The surface chemical composition of the prepared samples was examined using X-ray photoelectron spectroscopy (XPS; Multilab 2000 instrument, Thermo Fisher Scientific) with monochromated Al-Kα radiation (hν = 1486.6 eV). The C 1s peak located at around 285 eV was employed to calibrate the binding energies. The surface property was studied using the nitrogen gas adsorption/desorption technique on a Micromeritics Tristar 3000 analyzer. The Raman spectra were obtained from a LabRam ARAMIS IR2 spectrometer. Electron spin resonance (ESR) spectra were achieved by a JEOL JES-X320 system.

### 2.4. Electrochemical measurements

The electrochemical properties were evaluated using a standard three-electrode system (CHI660E, electrochemical workstation) in an alkaline medium. Catalyst (5 mg), carbon black (XC-72, 5 mg), and 5 wt % of the Nafion solution (0.2 mL) were introduced in 1.8 mL of the mixture of 2-propanol and distilled water (1:1 vol ratio) and sonicated for 1 h to prepare the working electrode. The catalyst ink was slowly deposited on a nickel foam (NF) substrate (1 × 1 cm<sup>2</sup>) and dried at 25 °C for 12 h. For the HER performance evaluation, linear sweep voltammetry (LSV) was conducted in the 1 M KOH electrolyte at a scan rate of 10 mV s<sup>-1</sup>. Ag/AgCl and Pt mesh were used as the reference and counter electrodes, respectively, to investigate HER activity, and the data were corrected with IR compensation of 95%. The cyclic voltammetry (CV) was performed at 20, 40, 60, 80, and 100 mV s<sup>-1</sup> scan rates in a non-faradaic potential range to analyze electrochemical active surface area (ECSA). The electrochemical impedance spectroscopy (EIS) was conducted from 0.1 Hz to 100 kHz. The stability of working electrodes was evaluated for 30 h by the chronoamperometric technique in a 1 M KOH medium. The obtained potentials were converted to a reversible hydrogen electrode (RHE) using the following equation:

$$E_{(\text{RHE})} = E_{(\text{Ag}/\text{AgCl})} + E_{(\text{Ag}/\text{AgCl})}^0 + 0.059 \times \text{pH}$$

### 2.5. DFT calculations

We performed spin polarized density functional theory (DFT)

calculations with the generalized gradient approximation (GGA)-level of exchange-correlation treatment (Perdew–Burke–Ernzerhof functional) [46] using the Vienna ab-initio simulation package (VASP) [47] and the DFT-D3 van der Waals correction method [48] with Becke–Johnson damping model to improve the reliability of the results. The interactions between the ionic cores and the valence electrons were described with the projector-augmented wave method (PAW). A plane-wave basis up to 400 eV of an energy cutoff was applied to construct the valence electron wave functions. To appropriately treat the localized Ce 4 *f* orbitals, the Hubbard *U* formalism with a  $U_{\text{eff}}$  of 4.5 eV was applied to the Ce ion [49,50]. The Brillouin zone was sampled at the  $\Gamma$ -point. The convergence criterion for the electronic and geometric optimization was set to  $10^{-4}$  eV and 0.03 eV/Å, respectively. We used

Gaussian smearing with a finite window of 0.05 eV to improve the convergence of the states near the Fermi level.

The N atoms are prone to preferentially incorporating Pyridinic-3 N motifs in the vicinity of carbon defects. Therefore, we modeled the N-doped graphene (NGr) using two types of bonding configurations, the N atom in constituting six-membered rings (Pyridinic-3 N) and in the basal plane of graphene (Graphitic-N), independently. The pristine-CeO<sub>2</sub> (111) and La-doped-CeO<sub>2</sub>(111) were modeled as (6 × 6) slab with six atomic layers, which was used in our previous study. The bottom layer of O–Ce–O was fixed during optimization, and a single NGr layer (9 × 9) composed of the two configurations of N atoms in graphene was supported on CeO<sub>2</sub>(111) surface and La-doped CeO<sub>2</sub>(111), respectively.

To evaluate HER activity, we calibrated the DFT-calculated hydrogen

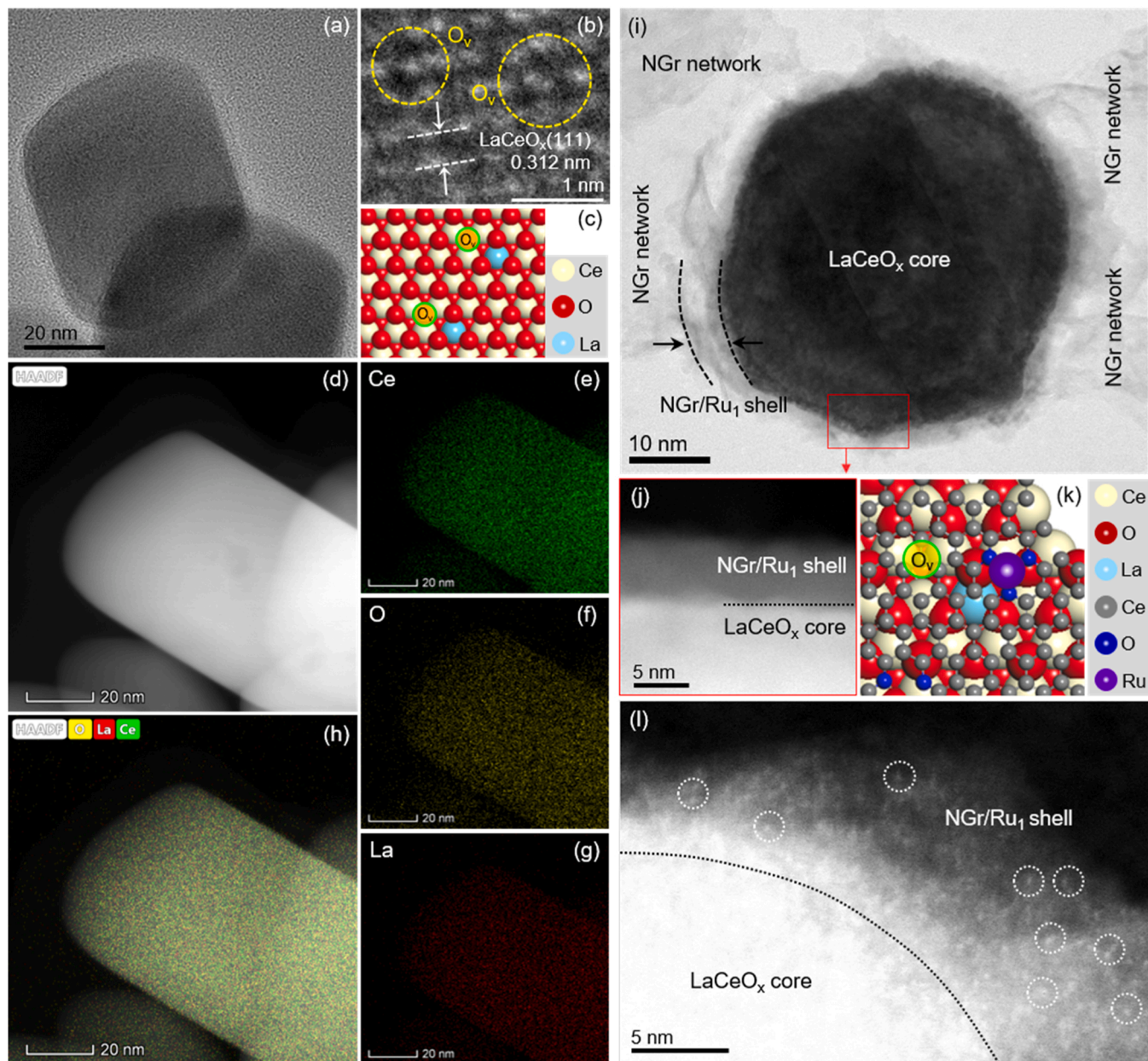


**Fig. 1.** (a) Bright-field TEM image of free-standing LaCeO<sub>x</sub> entity, (b) La-dopant-induced oxygen vacancy ( $O_v$ ) on the surface of LaCeO<sub>x</sub> (111) plane, as highlighted by the yellow circles, and (c) Top view of the DFT-optimized structure for the LaCeO<sub>x</sub> entity. (d) High-angle annular dark-field scanning transmission electron microscopy (HAADF-STEM) image of free-standing LaCeO<sub>x</sub> and (e–h) their STEM-EDS elemental maps: green (Ce), yellow (O), red (La), and overlaid maps. (i) Dark-field TEM image of LaCeO<sub>x</sub>@NGr/Ru<sub>1</sub> core-shell nanoparticles sitting on the NGr network. (j) High resolution TEM image at the interface of LaCeO<sub>x</sub>@NGr/Ru<sub>1</sub> core-shell structure. (k) Top view of the DFT-optimized structure for the LaCeO<sub>x</sub>@NGr/Ru<sub>1</sub>. (l) A typical HAADF-STEM observation at the interface of LaCeO<sub>x</sub> (brighter region) and NGr/Ru<sub>1</sub> components at which the dense Ru SAs implanted in NGr shell are indicated by the white circles.



adsorption energy to Gibbs free energy of hydrogen binding ( $\Delta G_{H^*}$ ). The Gibbs free energy is presented as:

$$\Delta G_{H^*} = E_{H^*} + \Delta E_{ZPE} - T\Delta S$$

Where  $E_{H^*}$  is the DFT-calculated adsorption energy of atomic hydrogen on the catalyst models,  $\Delta E_{ZPE}$  is the difference corresponding to the zero-point energy between gas-phase hydrogen and adsorbed hydrogen, and  $\Delta S$  represents the entropy contribution of  $H^*$  adsorption. Because the entropy of adsorbed hydrogen is negligibly small, we consider the entropy of hydrogen in the gas phase ( $S_0$  is the entropy of  $H_2$  in the gas phase at standard conditions, 1 bar of  $H_2$  and pH=0 at 300 K). Therefore, the free energy of hydrogen binding can be expressed [51]:

$$\Delta G_{H^*} = E_{H^*} + 0.24\text{eV}.$$

### 3. Results and discussion

#### 3.1. Characterizations

The synthesis process of the  $\text{LaCeO}_x @ \text{NGr}/\text{Ru}_1$  binary-site catalyst is demonstrated in Fig. S1 (Supplementary Material). The  $\text{LaCeO}_x$  core was first produced via a hydrothermal process and then hybridized with the  $\text{NGr}/\text{Ru}_1$  shell by pyrolysis. Fig. 1a displays a high-resolution TEM image of the as-calcined  $\text{LaCeO}_x$  material. Substituting  $\text{La}^{3+}$  ions in ceria could convert the  $\text{Ce}^{4+}$  ions into  $\text{Ce}^{3+}$  species to preserve charge neutrality. Further, the oxygen vacancies ( $\text{O}_v$ ) were simultaneously produced on the (111) surface of as-obtained  $\text{LaCeO}_x$  particles [52], as indicated by the yellow circles in Fig. 1b. Notably, after coupling with La dopant, the shape of the initial  $\text{CeO}_2$  host was well-preserved. In contrast, the surface area was possibly expanded due to the formation of oxygen defects. The DFT results further simulated the coexistence of La dopants and  $\text{O}_v$  species in  $\text{LaCeO}_x$  (Fig. 1c). High-resolution TEM analysis of pure  $\text{CeO}_2$  is provided in Fig. S2. A (111) surface of  $\text{CeO}_2$  (without defect) was ideally obtained accordingly. Fig. 1d presents a high-angle annular dark-field scanning transmission electron microscopy (HAADF-STEM) image of the as-calcined  $\text{LaCeO}_x$ . The corresponding energy dispersive X-ray spectroscopy (EDX) elemental analysis of as-prepared  $\text{LaCeO}_x$  is presented in Fig. 1(e-g), where the Ce, O, and La were mapped in green, yellow, and red, respectively. Their relevant overlaid composition is shown in Fig. 1h. Fig. 1i represents a typical high-resolution TEM image of the as-prepared composites, composed of  $\text{LaCeO}_x @ \text{NGr}/\text{Ru}_1$  core-shell particles intercalated between multi-wrinkled  $\text{NGr}$  networks. The thickness of the  $\text{NGr}/\text{Ru}_1$  shell on the  $\text{LaCeO}_x @ \text{NGr}/\text{Ru}_1$  structure was approximately 5 nm (Fig. 1i and j). So, the  $\text{NGr}$  network could improve the conductivity of the as-obtained nanohybrid system. The EDX elemental mapping and relevant spectrum of the as-prepared  $\text{LaCeO}_x @ \text{NGr}/\text{Ru}_1$  is supplemented in Fig. S3, in which the presence of Ce, O, La, C, N, and Ru is detected in blue, orange, green, red, slight-blue, and yellow, respectively. The core-shell structure of  $\text{LaCeO}_x @ \text{NGr}/\text{Ru}_1$  catalyst is further reinforced by line scanning profile. Fig. 1k displays the DFT-optimized  $\text{LaCeO}_x @ \text{NGr}/\text{Ru}_1$  core-shell platform structure. The HAADF-STEM image of the  $\text{NGr}/\text{Ru}_1$  constituent using the probe Cs corrector is shown in Fig. 1l, in which the isolated Ru single atoms anchored on the  $\text{NGr}$  shell are marked by white circles. In this picture, the presence of the isolated  $\text{Ru}^0$  or  $\text{Ru}^{\delta+}$  single-atoms is further evidenced by room-temperature CO DRIFTS, Fig. S4. Under CO environment, the band located at  $2058\text{ cm}^{-1}$  is contributed to linearly adsorbed CO on these well-dispersed Ru single-atom species on the surface of  $\text{LaCeO}_x @ \text{NGr}$  host, in line with the literature [53,54]. Our previous reports showed that the former freeze-drying step helped well-disperse  $\text{Ru}^{3+}$  species in the  $\text{NGr}$  precursor network [33,34]. Subsequently, the electron-rich N dopants favorably reduced metallic ions to their single-atom forms ( $\text{Ru}^{3+} \rightarrow \text{Ru}^0$ ), forming the active Ru- $\text{N}_3$  sites during the latter pyrolysis process. The conclusion is in line with very recent studies where the coordination number of Ru is also 3 [55–57]. In particular, the Ru–Ru bonding was

not observable in the surface of  $\text{LaCeO}_x @ \text{NGr}$  [58]. For comparison, the TEM image of free-standing  $\text{NGr}$  is also shown in Fig. S5. As seen in Fig. S6, the defect-rich  $\text{LaCeO}_x$  surface exhibited a higher nitrogen adsorption/desorption capacity than pure  $\text{CeO}_2$ . In particular, when hybridized with the  $\text{NGr}/\text{Ru}_1$  shell, the obtained  $\text{LaCeO}_x @ \text{NGr}/\text{Ru}_1$  material had the best behavior. This could be attributed to the material's high porosity from ice crystals' sublimation during freeze-drying. Accordingly, the order of Brunauer–Emmett–Teller (BET) specific surface area was determined:  $\text{LaCeO}_x @ \text{NGr}/\text{Ru}_1$  ( $103\text{ m}^2\text{ g}^{-1}$ ) >  $\text{LaCeO}_x$  ( $50\text{ m}^2\text{ g}^{-1}$ ) >  $\text{CeO}_2$  ( $46\text{ m}^2\text{ g}^{-1}$ ). A twofold surface-area increase of  $\text{LaCeO}_x @ \text{NGr}/\text{Ru}_1$  would expose a large number of active sites for catalytic reactions. TEM images of  $\text{LaCeO}_x @ \text{NGr}$  and  $\text{CeO}_2 @ \text{NGr}/\text{Ru}_1$  materials are also shown in Fig. S7 and S8. The mass loading of Ru single atoms in  $\text{CeO}_2 @ \text{NGr}/\text{Ru}_1$  and  $\text{LaCeO}_x @ \text{NGr}/\text{Ru}_1$  was constantly kept at 1.5 wt%.

In Fig. 2a, XRD patterns of as-prepared  $\text{CeO}_2$  and  $\text{LaCeO}_x$  are perfectly indexed to the cubic fluorite  $\text{CeO}_2$  structure (JCPDS No. 04–0593). The sharpened diffraction peaks indicate a high crystallinity degree. The absence of impurity peaks demonstrates that the La dopants in the  $\text{La}^{3+}$  state were atomically dispersed in the ceria host without creating the segregated  $\text{La}_2\text{O}_3$ . The cubic fluorite phase of the ceria host was also well-preserved as introducing the  $\text{La}^{3+}$ . However, a magnified view of the (111) peak presented a visible shift towards a lower angle after doping (that is,  $28.48$ – $28.41^\circ$  (2 $\theta$ )). This phenomenon signifies lattice expansion due to substituting larger  $\text{La}^{3+}$  ions into the crystal structure of the  $\text{CeO}_2$  host. The appearance of oxygen vacancies further contributed to the crystal growth of  $\text{LaCeO}_x$  [59]. The expansion in the crystal structure was exceptionally advantageous for surface area increment, as confirmed by the previous specific surface area measurements and electronic transmission [60]. After surface hybridization with the  $\text{NGr}/\text{Ru}_1$ -containing shell, the XRD peaks of  $\text{LaCeO}_x$  and  $\text{NGr}$  constituents appeared, as shown in Fig. S9. This hybridization is also a reason for the appearance of the new Ce–N bridge at  $31.1^\circ$  [61], between the  $\text{LaCeO}_x$  core and  $\text{NGr}/\text{Ru}_1$  shell, in line with the following XPS analysis. However, the Ru SAs phases could not be particularly measurable in the XRD pattern. This suggests a perfect contribution of Ru single atoms in the  $\text{LaCeO}_x @ \text{NGr}/\text{Ru}_1$ .

In addition, electron paramagnetic resonance (EPR) was recorded at room temperature to clarify experimental evidence of defects in ceria-based materials (Fig. 2b).  $\text{CeO}_2$  and  $\text{LaCeO}_x$  materials exhibited a resonance signal at  $g = 2.002$ , probably due to the presence of oxygen vacancies. However, the La-doped ceria had a stronger resonance than  $\text{CeO}_2$ , indicating a higher  $\text{O}_v$  concentration. The  $\text{O}_v$  concentration increment in  $\text{LaCeO}_x$  compared to  $\text{CeO}_2$  was also investigated by Raman-scattering spectra (Fig. 2c). In  $\text{CeO}_2$ , the frequency at  $466\text{ cm}^{-1}$  is characteristic of the  $\text{F}_2\text{g}$  symmetry and can be considered a symmetric stretching mode of oxygen around each cation [62]. As shown in the inset of the figure, a slight shift of the  $\text{F}_2\text{g}$  mode towards a lower frequency was detected in the  $\text{LaCeO}_x$  material. Hence, it indicates a decline in oxygen atoms around cerium ions and, thus, an increment in oxygen vacancies [63]. The other broad  $\text{D}_1$  and  $\text{D}_2$  modes (peaked at  $535$  and  $598\text{ cm}^{-1}$ ) are attributed to the presence of  $\text{O}_v$  species. The former is related to the extrinsic  $\text{O}_v$  ordering caused by La dopant, while the latter is the intrinsic  $\text{O}_v$  ones induced by high-temperature calcination. The  $\text{LaCeO}_x$  presented a higher  $\text{D}_1$  intensity than  $\text{CeO}_2$ , thus enriching total  $\text{O}_v$  species in doped ceria, in line with the EPR and XPS analyses. DFT calculations further clarified the experimental oxygen vacancy formation in  $\text{CeO}_2$  and  $\text{LaCeO}_x$  with the corresponding optimized structures in Fig. 2(d and e). It is clear that when La is introduced into the  $\text{CeO}_2$  matrix, the oxygen vacancy formation energy dramatically decreases compared with undoped  $\text{CeO}_2$ , from 2.7 eV to 1.1 eV.

XPS investigations for  $\text{CeO}_2$  and  $\text{LaCeO}_x$  materials are presented in Fig. S10a (Supplementary Material), indicating the presence of Ce, O, and La elements. Fig. S10b presents the deconvoluted La 3d XPS spectrum of the  $\text{LaCeO}_x$  sample, consisting of  $\text{La } 3d_{5/2}$  and  $\text{La } 3d_{3/2}$ . The spectrum also indicates that the La dopant existed in the +3 oxidation state



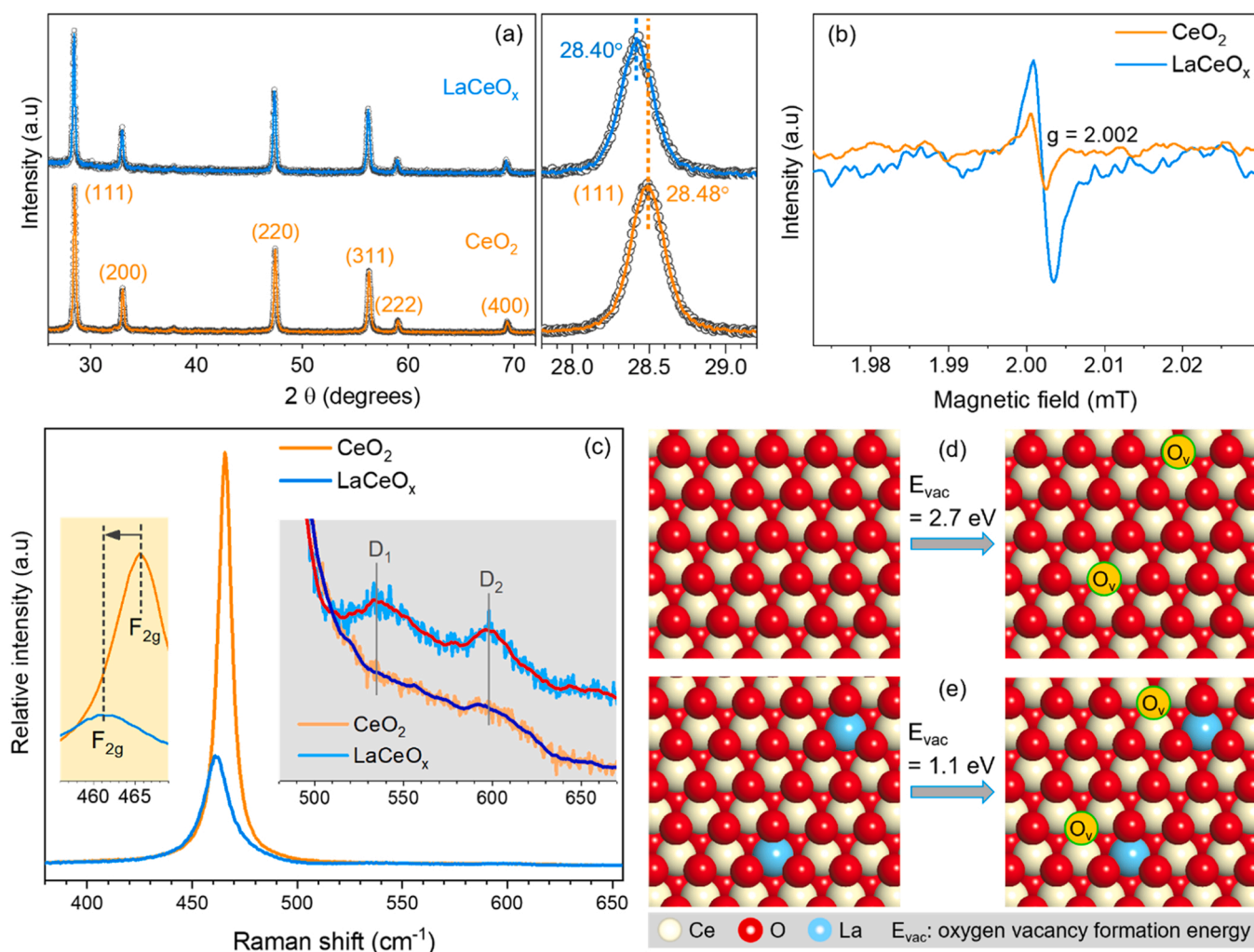


**Fig. 2.** Characterizations for  $\text{CeO}_2$  and  $\text{LaCeO}_x$ : (a) representative XRD pattern, (b) EPR spectra measurements with a microwave frequency of 9.6 GHz, and (c) Raman-scattering spectra obtained at 457.9 nm laser excitation line. (d and e) DFT-calculated results for the required energy for one oxygen vacancy formation in  $\text{CeO}_2$  and  $\text{LaCeO}_x$  materials.

[64]. In addition, the high-resolution XPS spectrum of O 1s for undoped  $\text{CeO}_2$  and  $\text{LaCeO}_x$  is shown in Fig. S10c, fitted into two peaks: lattice oxygen ( $\text{O}^{2-}$ : blue) and chemisorbed oxygen species ( $\text{O}_c$ : red) [65].  $\text{LaCeO}_x$  exhibited a higher  $\text{O}_c/\text{O}^{2-}$  ratio than undoped  $\text{CeO}_2$ . This suggests the increment of  $\text{O}_v$  concentration in doped one [66], matching previous Raman and EPR analyses. The high-resolution XPS of the Ce 3d level for undoped  $\text{CeO}_2$  and  $\text{LaCeO}_x$  was divided into 8 peaks according to their valence states:  $\text{Ce}^{3+}$  and  $\text{Ce}^{4+}$  (Fig. S10d). The La-doping caused the peak shift towards higher binding energies. The concentration of  $\text{Ce}^{3+}$  species was calculated by integrating  $\text{Ce}^{3+}$  bands for the total area of the Ce 3d spectrum, which was 7.4% for  $\text{CeO}_2$  and 16.7% for  $\text{LaCeO}_x$ , respectively (Fig. S10e). The increase in  $\text{Ce}^{3+}$  species resulted from the enrichment of oxygen vacancies in the doped material. XPS analysis for  $\text{LaCeO}_x$  @NGR/ $\text{Ru}_1$  is also displayed in Fig. S11a, confirming the presence of all elements. In Fig. S11b, the N 1s profile is deconvoluted into four peaks: pyridinic, pyrrolic, graphitic, and oxidized nitrogen, respectively [67]. The oxidized-N bond peak demonstrates the coordination between N species in NGR and metallic sites in Ru single atoms and  $\text{LaCeO}_x$ , reinforcing the nature of electronic interactions between these three constituents in  $\text{LaCeO}_x$  @NGR/ $\text{Ru}_1$ . The XPS analysis for C 1s and Ru 3d in  $\text{LaCeO}_x$  @NGR/ $\text{Ru}_1$  is further represented in Fig. S11c. The high-resolution spectrum of Ru 3d, which partially overlapped with C 1s, was divided into Ru  $3d_{5/2}$  and  $3d_{3/2}$  components. It indicates the coexistence of  $\text{Ru}^{3+}$  and  $\text{Ru}^0$  valence states.

### 3.2. Electrochemical measurements

The HER activity of the as-prepared catalysts was evaluated by linear scanning voltammetry (LSV) using a standard three-electrode setup in the 1.0 M KOH electrolyte with a scan rate of  $10 \text{ mV s}^{-1}$ . Commercial Pt/C (20 wt% Pt) was considered as the reference. Undoubtedly, the electrochemical properties of as-synthesized catalysts were significantly enhanced with the oxygen vacancy increment due to La doping. In the typical LSV performance (with iR compensation), the  $\text{LaCeO}_x$  @NGR/ $\text{Ru}_1$  was superior performance among the  $\text{CeO}_2$ -containing materials (Fig. 3a). It exhibited smaller overpotentials (22 and 95 mV vs. RHE) at current densities of 10 and  $100 \text{ mA cm}^{-2}$  compared to  $\text{CeO}_2$  @NGR/ $\text{Ru}_1$  (42 and 170 mV),  $\text{LaCeO}_x$  @NGR (100 and 210 mV),  $\text{LaCeO}_x$  (140 and 250 mV), and  $\text{CeO}_2$  (165 and 275 mV) materials, and close to commercial Pt/C (17 and 60 mV) (Fig. 3b). Fig. 3c presents the Tafel slope of the catalysts according to the as-achieved iR-corrected LSV response. The slopes were  $34 \pm 1.34$ ,  $40 \pm 1.01$ ,  $67 \pm 0.13$ ,  $72 \pm 0.26$ ,  $75 \pm 0.16$ , and  $95 \pm 0.21 \text{ mV dec}^{-1}$  for Pt/C,  $\text{LaCeO}_x$  @NGR/ $\text{Ru}_1$ ,  $\text{CeO}_2$  @NGR/ $\text{Ru}_1$ ,  $\text{LaCeO}_x$  @NGR,  $\text{LaCeO}_x$ , and  $\text{CeO}_2$ , respectively. The Tafel slope of  $\text{LaCeO}_x$  @NGR/ $\text{Ru}_1$  was somewhat greater than but close to Pt/C. This indicates a fast rate-determining step over the dual-site catalyst toward HER [68]. In addition, the exchange current density ( $j_0$ ) was evaluated for each catalyst (Fig. S12). The  $j_0$  value is  $3.5 \times 10^{-4} \text{ A cm}^{-2}$  for  $\text{LaCeO}_x$  @NGR- $\text{Ru}_1$ , standing out the performance of  $\text{CeO}_2$  @NGR- $\text{Ru}_1$

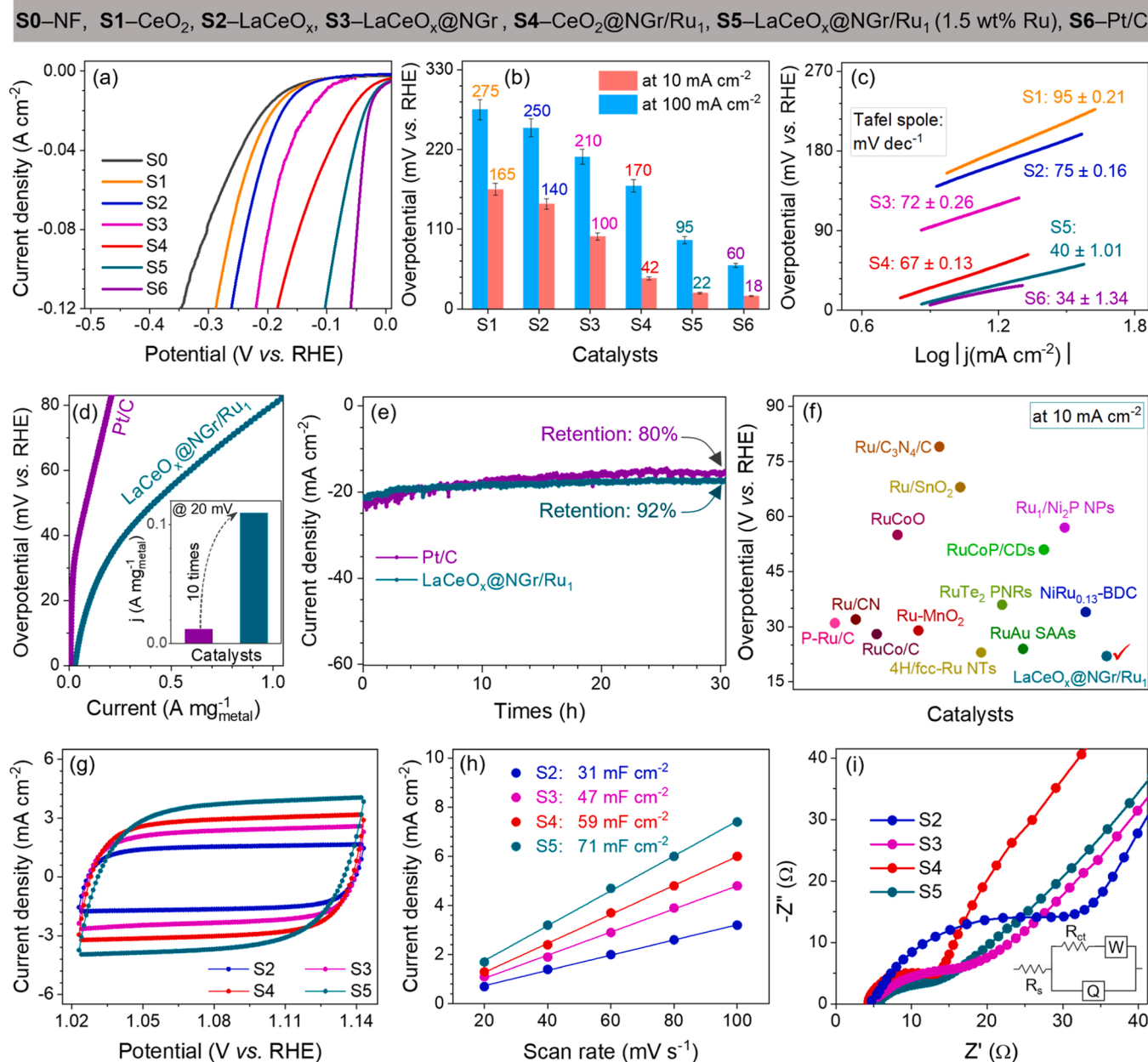


**Fig. 3.** (a) LSV curves (with iR compensation of 95%) of the as-fabricated catalysts for HER activity in 1.0 M KOH electrolyte at a scan rate of 10 mV s<sup>-1</sup>, (b) relevant HER overpotentials at current density of 10 and 100 mA cm<sup>-2</sup>, (c) Tafel slopes and (d) mass activity normalized by the metal mass loading according to the as-obtaining LSV measurements for different materials. (e) 30-h long-term chronoamperometric HER stability over an advanced LaCeO<sub>x</sub>@NGr/Ru<sub>1</sub> catalyst and commercial Pt/C entity. (f) Comparison HER overpotentials of LaCeO<sub>x</sub>@NGr/Ru<sub>1</sub> binary-site entity and the recently Ru-advanced catalysts at a current density of 10 mA cm<sup>-2</sup>. (g) CV polarizations at a sweep rate of 100 mV s<sup>-1</sup> and (h) C<sub>dl</sub> slope analysis at different scan rates of the as-fabricated catalysts in 1.0 M KOH medium. (i) EIS analysis for the as-obtained materials in a frequency range of 10<sup>5</sup> to 10<sup>-2</sup> Hz.

(1.8 × 10<sup>-4</sup> A cm<sup>-2</sup>), LaCeO<sub>x</sub>@NGr (2.5 × 10<sup>-5</sup> A cm<sup>-2</sup>), LaCeO<sub>x</sub> (2.0 × 10<sup>-5</sup> A cm<sup>-2</sup>), and CeO<sub>2</sub> (1.6 × 10<sup>-5</sup> A cm<sup>-2</sup>), respectively. It is further comparable to the unbeatable Pt/C catalyst for HER: 4.0 × 10<sup>-4</sup> A cm<sup>-2</sup> [69]. The synergistic effect of the LaCeO<sub>x</sub> core and NGr shell could upgrade the utilization of the Ru catalytic active sites based on the HER mass activity (Fig. 3d). As shown in the inset of the figure, the LaCeO<sub>x</sub>@NGr/Ru<sub>1</sub> catalyst delivered a current mass activity of 110 mA mg<sub>Ru</sub><sup>-1</sup>, ~10 times superior to that obtained from Pt/C (10.9 mA mg<sub>Pt</sub><sup>-1</sup>) at an overpotential of 20 mV (vs. RHE). In addition, long-term stability is another essential parameter to reinforce the electrochemical activity of catalysts. In Fig. 3e, the binary-site LaCeO<sub>x</sub>@NGr/Ru<sub>1</sub> catalyst exhibited remarkable retention (92%) in HER activity during a 30-h run compared to Pt/C (retention of 80%) in a 1.0 M

KOH medium. It evidenced the long-lasting HER durability of LaCeO<sub>x</sub>@NGr/Ru<sub>1</sub> species. In Fig. 3f, the HER performance superiority of our catalyst is further compared with the recent Ru-containing advanced materials in an alkaline medium in terms of the overpotentials to generate a current density of 10 mA cm<sup>-2</sup>. On the other hand, the ECSA and charge mobility were determined to clarify insights into HER activity. In this picture, the ECSA value estimated by cyclic voltammetry (CV) is ordinarily proportional to its double-layer capacitance (C<sub>dl</sub>) [70]. The CV polarization at the different scan rates is given for four catalysts in Fig. S13-S16: LaCeO<sub>x</sub>, LaCeO<sub>x</sub>@NGr, CeO<sub>2</sub>@NGr/Ru<sub>1</sub>, and LaCeO<sub>x</sub>@NGr/Ru<sub>1</sub>. At a scan rate of 100 mV s<sup>-1</sup>, the LaCeO<sub>x</sub>@NGr/Ru<sub>1</sub> showed the largest calculated ECSA value from the CV results compared to CeO<sub>2</sub>@NGr/Ru<sub>1</sub>, LaCeO<sub>x</sub>, and CeO<sub>2</sub> (Fig. 3g). Yet, the LaCeO<sub>x</sub>



@NGr/Ru<sub>1</sub> reached a convenient double-layer capacitance value ( $C_{dl}$  slope/2, Fig. 3h) of  $35.5 \text{ mF cm}^{-2}$ , significantly higher than those of  $\text{CeO}_2$  @NGr/Ru<sub>1</sub> ( $29.5 \text{ mF cm}^{-2}$ ),  $\text{LaCeO}_x$  ( $23.5 \text{ mF cm}^{-2}$ ), and  $\text{CeO}_2$  ( $15.5 \text{ mF cm}^{-2}$ ), even comparable to that of Pt/C ( $40.0 \text{ mF cm}^{-2}$ , Fig. S17). It suggests that  $\text{LaCeO}_x$  @NGr/Ru<sub>1</sub> provided plenty of active sites for improving HER activity. The charge transfer resistance ( $R_{ct}$ ) in the as-prepared catalysts was further verified by the electrochemical impedance spectroscopy (EIS) measurement. In Fig. 3i, the  $R_{ct}$  value is approximately  $10 \Omega$  for  $\text{LaCeO}_x$  @NGr/Ru<sub>1</sub>,  $12 \Omega$  for  $\text{CeO}_2$  @NGr/Ru<sub>1</sub>,  $22 \Omega$  for  $\text{LaCeO}_x$  @NGr, and  $40 \Omega$  for  $\text{LaCeO}_x$ , respectively, determined from the diameter of the semicircle fitted with a suitable equivalent circuit in the figure. Accordingly, the  $\text{LaCeO}_x$  @NGr/Ru<sub>1</sub> produced a smaller resistance among the as-prepared materials. This possibly facilitated charge mobility at the interfacial electrolyte-electrode contact, thus fastening electrocatalytic kinetics towards HER in an alkaline medium [71]. The post-HER  $\text{LaCeO}_x$  @NGr/Ru<sub>1</sub> catalyst is recharacterized after a long-stability test. In Fig. S18, the phase of the as-used

material is well-preserved compared to the fresh one. However, some impurity noise can also be observed in XRD pattern, possibly due to the presence of carbon black support and nafion binder. From TEM observation in Fig. S19, the core-shell morphology of  $\text{LaCeO}_x$  @NGr/Ru<sub>1</sub> catalyst is perfectly maintained, indicating the excellent stability of the post sample. The presence of all elements (Ce, O, La, C, N, and Ru) is further evidenced by XPS spectrum, even the deposition of an ultralow Pt species on the surface catalyst is also detectable but negligible on the post-HER sample after a long-term run in an alkaline medium, Fig. S20.

### 3.3. DFT calculation and HER mechanism

DFT calculations were performed to clarify the properties of the catalysts evaluated in the previous sections. Electronic interactions and hydrogen adsorption have been considered for the materials studied experimentally. We constructed various models and optimized them: NGr,  $\text{CeO}_2$ ,  $\text{LaCeO}_x$ ,  $\text{CeO}_2$  @NGr/Ru<sub>1</sub>, and  $\text{LaCeO}_x$  @NGr/Ru<sub>1</sub> species

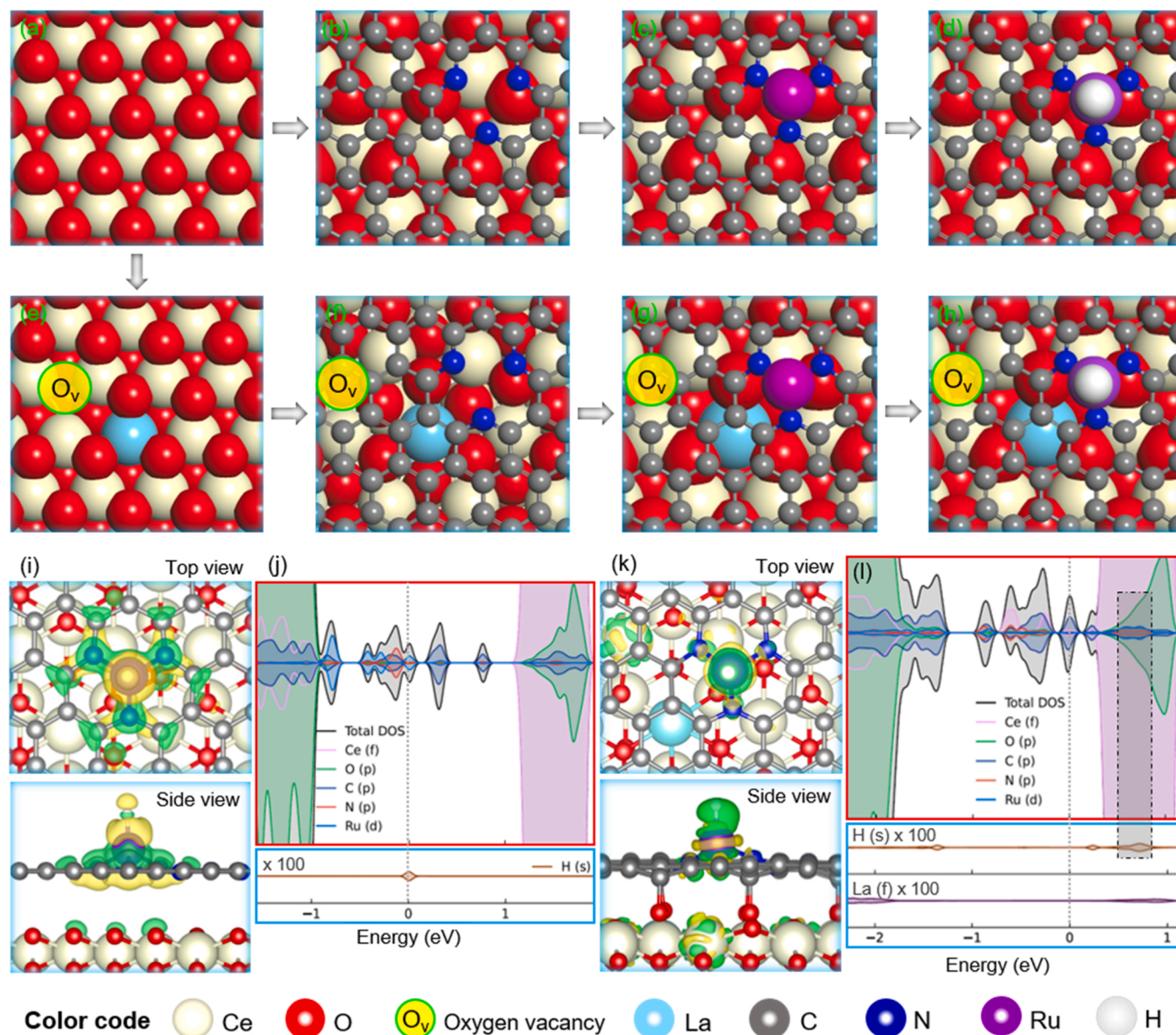


**Fig. 4.** (a-c and e-f) Top view of optimized structural determination for  $\text{CeO}_2(111)$  @NGr/Ru<sub>1</sub> and  $\text{LaCeO}_x(111)$ /NGr-Ru<sub>1</sub> from  $\text{CeO}_2(111)$  and  $\text{LaCeO}_x(111)$  entities. (d and h) A H atom adsorption on  $\text{CeO}_2(111)$  @NGr/Ru<sub>1</sub> and  $\text{LaCeO}_x(111)$  @NGr/Ru<sub>1</sub>. Top and side views for charge density difference analysis in a H adsorbed on (i)  $\text{CeO}_2(111)$  @NGr/Ru<sub>1</sub> and (k)  $\text{LaCeO}_x(111)$  @NGr/Ru<sub>1</sub> models with an isosurface-value of  $0.03 \text{ e}/\text{\AA}^3$ . Charge accumulation and depletion regions are described in green and yellow, respectively. (j and l) Red boxes represent density of states (DOS) of the optimized  $\text{CeO}_2(111)$  @NGr/Ru<sub>1</sub>-H and  $\text{LaCeO}_x(111)$  @NGr/Ru<sub>1</sub>-H structures, and blue ones are the DOS data of H (s) and La (f) states with a magnification of 100.



with their top views are illustrated in Fig. 4(a-h) and S21. Adsorption of a hydrogen atom was considered for the best HER catalysts:  $\text{CeO}_2$  @NGr/ $\text{Ru}_1$  and  $\text{LaCeO}_x$  @NGr/ $\text{Ru}_1$ , as shown in Fig. 4(d and h). We also visualized the charge density difference for an H adsorbed on  $\text{CeO}_2$  @NGr/ $\text{Ru}_1$  and  $\text{LaCeO}_x$  @NGr/ $\text{Ru}_1$ . In Fig. 4i, the oxygen vacancy deficiency in the  $\text{CeO}_2$  could weaken the electronic interactions between  $\text{CeO}_2$  and NGr/ $\text{Ru}_1$  components [66]. In particular, the electrons depleted from adsorbed H species (yellow areas) were apparently accumulated in the NGr/ $\text{Ru}_1$  shell along the  $\text{Ru}_1$ -N<sub>3</sub> bond (green areas). Although this possibly helps to stabilize Ru SAs on the  $\text{CeO}_2$  @NGr heterostructure surface, but also strengthens the  $\text{Ru}_1$ -H\* bond, thus inhibiting  $\text{H}_2$  evolution on the  $\text{CeO}_2$  @NGr/ $\text{Ru}_1$  catalyst. In contrast, the electronic interactions between defect-rich  $\text{LaCeO}_x$  and NGr/ $\text{Ru}_1$  could facilitate charge transfer in these constituents (Fig. 4k). The free electron density was much enriched around Ru SAs anchored on  $\text{LaCeO}_x$  @NGr compared to that of  $\text{CeO}_2$  @NGr. Subsequently, the metallic species provided more electrons for adsorbed H atoms along the  $\text{Ru}_1$ -H\* bonds (green areas) to promote  $\text{H}_2$  production on the binary-site  $\text{LaCeO}_x$  @NGr/ $\text{Ru}_1$  catalyst. In addition, the DFT-calculated density of states (DOS) of  $\text{CeO}_2$  @NGr/ $\text{Ru}_1$  and  $\text{LaCeO}_x$  @NGr/ $\text{Ru}_1$  are shown in Fig. 4(j and l). The defect-less  $\text{CeO}_2$  core dramatically increased the electron density of Ru 3d orbitals below the Fermi level towards  $\text{Ru}_1$ -N<sub>3</sub> coupling (Fig. 4j). Meanwhile, the La-doped catalyst exhibited higher occupation, indicating an accelerated electron transfer and better conductivity. The expanded DOS of  $\text{LaCeO}_x$  @NGr/ $\text{Ru}_1$  near the Fermi level is probably attributed to the Ce 4f orbitals of  $\text{Ce}^{3+}$  species. It means that doping La into ceria could increase the influence of the 4f electrons, favoring water adsorption and dissociation. Furthermore, the DOS profile of  $\text{LaCeO}_x$  @NGr/ $\text{Ru}_1$  depicted an overlapping at around 0.7 V, possibly due to the Ru 3d/H 1s hybridization (Fig. 4l). It also suggests that the

electrons from  $\text{Ce}^{3+}$ -contained core (e.g., 4f orbital) were accumulated around the  $\text{Ru}_1$  site towards the  $\text{Ru}_1$ -H\* bond, thus favoring adsorption of hydrogen atoms [66] and facilitating  $\text{H}_2$  desorption over a dual-active-site catalyst via a spillover mechanism.

According to the Tafel slope in Fig. 3c, the 40 mV dec<sup>-1</sup> indicates that the best HER binary-site  $\text{LaCeO}_x$  @NGr/ $\text{Ru}_1$  catalyst exhibited a Volmer-Tafel mechanism via the hydrogen spillover, which could be verified by Gibbs free energies. The former reaction,  $\text{H}_2\text{O} + \text{e}^- \rightarrow \text{HO}^- + \text{H}^*$ , is activated by the ceria-related species as a crucial step to generate protons and is possibly governed by the oxygen vacancy. Thus, DFT calculations were considered to reinforce these conclusions. We adsorbed a water molecule on the oxygen vacancy at  $\text{CeO}_2$ (111) and  $\text{LaCeO}_x$ (111) models (Fig. S22a). The calculated water binding energy ( $E_{\text{bind}}$ ) and relevant dissociation free energy ( $\Delta E$ ) are -0.96 and -1.36 eV for  $\text{CeO}_2$  and -0.84 and -1.43 eV for  $\text{LaCeO}_x$ , respectively. The dissociation of water is more favorable on the defect-rich  $\text{LaCeO}_x$  surface, probably due to the increment of the active sites, e.g., oxygen vacancy and  $\text{Ce}^{3+}$  species. In fact, the  $\text{O}_v$  species are greatly favorable to adsorb water [72], while the  $\text{O}_v$ -induced  $\text{Ce}^{3+}$  species later support dissociating water. In contrast, the high surface area N-doped graphene is unfavorable to adsorb and dissociate water (Fig. S22b) but can increase the conductivity of the catalyst obtained to speed of the moving of electrons for  $\text{H}^+ \rightarrow \text{H}^*$  conversion on defect-rich ceria species to participate subsequent reactions via a spillover mechanism (Fig. 5a). The latter Tafel reaction ( $\text{H}^* + \text{H}^* = \text{H}_2$ ) is the rate-determining step in the hydrogen diffusion [71]. Fig. 5b reports the Gibbs free energy of adsorption as the reaction descriptor for a hydrogen atom on the materials described: NGr,  $\text{CeO}_2$ ,  $\text{LaCeO}_x$ ,  $\text{LaCeO}_x$  @NGr,  $\text{CeO}_2$  @NGr/ $\text{Ru}_1$ , and  $\text{LaCeO}_x$  @NGr/ $\text{Ru}_1$  (as modeled in Fig. 4(d, h) and S23). According to the Sabatier principle, the perfect catalysts should adsorb adsorbates

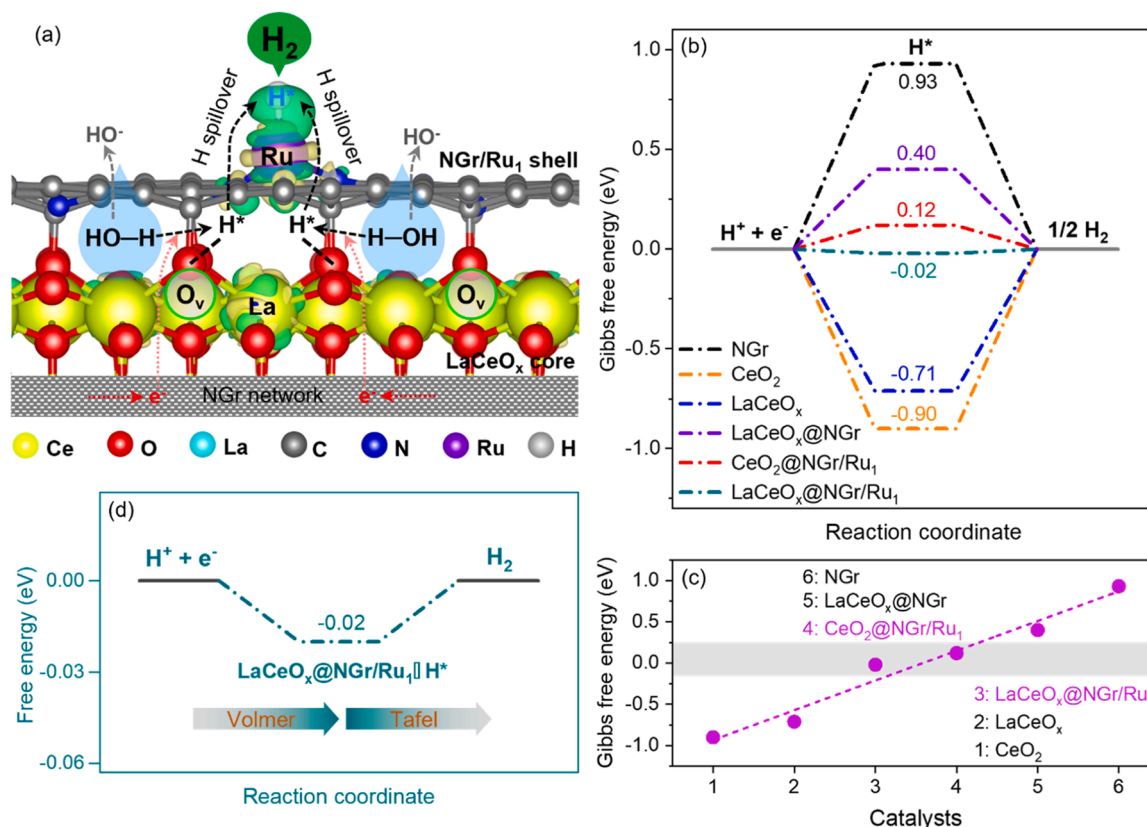


**Fig. 5.** (a) Possible hydrogen spillover mechanism for the alkaline HER over an advanced binary-site  $\text{LaCeO}_x$ @NGr/ $\text{Ru}_1$  catalyst. (b) Gibbs-computed free energy for a hydrogen adsorption on the various models: NGr,  $\text{CeO}_2$ (111),  $\text{LaCeO}_x$ (111),  $\text{CeO}_2$ (111)@NGr/ $\text{Ru}_1$ , and  $\text{LaCeO}_x$ (111)@NGr/ $\text{Ru}_1$  species. (c) Trend of the hydrogen adsorption free energy over the different catalysts described with the grey shaded region points out the emplacement of the ideal catalysts for alkaline HER in this work. (d) Corresponding reaction pathway during HER activity based on Gibbs free energy variation.

and reaction intermediates neither too strong nor too weak. It indicates that the single hydrogen atom should have free adsorption energy close to that of the precursor,  $H^+ + e^-$  (0 eV), and of the product,  $\frac{1}{2} H_2$  (0 eV). In this picture, free-standing NGr was particularly inactive because it delivered a positive  $\Delta G_H$  of 0.93 eV, suggesting weak H binding ability. The other extremes were  $CeO_2$  and  $LaCeO_x$  since they strongly bonded to H species (−0.90 and −0.71 eV, respectively). This agrees with the experimental observation since these are poor individual catalysts among the materials considered. However, the possibility differs as they were coupled to create an oxide@graphene-contained interface. For instance,  $LaCeO_x$ @NGr showed a  $\Delta G_H$  value of 0.40 eV, indicating a visible enhancement compared to its counterparts. The HER performance is further upgraded if the oxide@graphene structures are functionalized with a Ru single atom. Free energy reached an optimal value of 0.12 eV for  $CeO_2$ @NGr/ $Ru_1$  and −0.02 eV for  $LaCeO_x$ @NGr/ $Ru_1$ . Therefore, going from a  $CeO_2$ -containing catalyst to a defect-rich La-doped  $CeO_2$ -based one, the H adsorption free energy varied from 0.12 eV to −0.02 eV, in agreement with going from a modest to an excellent catalyst. Noted that the empty Pyridinic-3 N site models, NGr and  $LaCeO_x$ @NGr without Ru SAs (Fig. S24), exhibited significantly high free adsorption energies of hydrogen, −2.00 eV and −3.56 eV, respectively. Such sites of 3 N configuration in free-standing NGr and  $LaCeO_x$ @NGr were inevitably deactivated due to strongly adsorbed hydrogen. Thus, the active site of catalysts without Ru SAs for HER is the vicinity site of Graphitic-N, which shows relatively weaker binding energies of hydrogen atom than that of the Pyridinic-3 N sites. Consequently, the  $Ru_1$ -functionalized  $LaCeO_x$ @NGr model could adsorb a hydrogen atom by an optimal exothermic reaction to facilitate the Tafel reaction, even superior to the state-of-art (111) Pt surface [33]. Fig. 5c displays the trend of the as-obtained Gibbs hydrogen adsorption free energy over the materials considered: NGr,  $CeO_2$ ,  $LaCeO_x$ ,  $LaCeO_x$ @NGr,  $CeO_2$ @NGr/ $Ru_1$ , and  $LaCeO_x$ @NGr/ $Ru_1$ . Noted that there is a linear correlation between the capability to bind  $H^*$  species and the catalyst. The plot indicates the ideal catalysts in grey shaded area for binary-site entities. According to the DFT calculations, we proposed a plausible hydrogen spillover for Volmer-Tafel mechanism over  $LaCeO_x$ @NGr/ $Ru_1$  catalyst. Because of a large difference in the work function between NGr and  $LaCeO_x$  species, the access electron on N-sites in NGr/ $Ru_1$  shell will transfer to  $LaCeO_x$  core for a  $Ce^{4+} \rightarrow Ce^{3+}$  reduction, forming the Ce-N bond when they are in close contact. In this picture, the formation of CeN bond can increase the concentration of active catalytic  $Ce^{3+}$  species, favorable for water adsorption and dissociation in Volmer step. On the other hand, the Ce-N bridge can accelerate the transfer of dissociated  $H^*$  intermediates from the core to shell, finally reaching the  $Ru_1$  surface via the  $Ce^{3+}$ -N- $Ru_1$  sites via the hydrogen spillover pathway. When  $H^*$  species reached the surface of the  $Ru_1$ -functionalized  $LaCeO_x$ @NGr catalyst, they were integrated into molecules for liberating hydrogen gas via the Tafel step (Fig. 5d). Thus, the binary-site  $LaCeO_x$ @NGr/ $Ru_1$  design approvingly facilitates water adsorption and dissociation, accelerating the diffusion of adsorbed  $H^*$  intermediates, and finally delivering a superior HER performance via the hydrogen diffusion.

#### 4. Conclusion

In this work, we reported the synthesis of an effective dual-site catalyst for alkaline HER composed of  $LaCeO_x$  and NGr/ $Ru_1$ .  $LaCeO_x$ @NGr/ $Ru_1$  provided three essential benefits for an overall HER efficiency according to the hydrogen spillover: O<sub>v</sub>-abundant  $LaCeO_x$  for facile water adsorption and splitting,  $Ce^{3+}$ -N- $Ru_1$  bond for the diffusion of as-associated  $H^*$  species, and Ru single-atom site for fast hydrogen gas desorption. With these intrinsic merits, the three-component  $LaCeO_x$ @NGr/ $Ru_1$  (1.5 wt% Ru) dual-site catalyst exhibited a remarkable HER performance: a low overpotential of 22 mV at 10 mA cm<sup>−2</sup> with a high exchange current density ( $3.5 \times 10^{-4}$  A cm<sup>−2</sup>) and a Tafel slope of 40 mV dec<sup>−1</sup> in an alkaline medium. It also delivered a high mass

activity of 110 mA mg<sub>Ru</sub><sup>−1</sup> at an overpotential of 20 mV and long-lasting durability after a 30-h stability test. Its performance was thus superior to the reported Ru-containing catalysts and commercial Pt/C (20 wt%). DFT calculations further reinforced the substantial contribution of oxygen vacancies, strong electronic interactions, and low hydrogen adsorption free energy in this system toward alkaline HER. This work shed new light on developing a versatile three-component catalyst: oxide-, graphene-, and single-atom-contained species with dual active sites for efficient and long-lasting hydrogen production reactions.

#### CRedit authorship contribution statement

**Vandung Dao:** Conceptualization, Methodology, Software, Formal analysis, Investigation, Resources, Data curation, Writing – original draft. **Hyuk Choi:** Software, Formal analysis, Data curation, Writing – original draft. **Sunny Yadav:** Data curation and Analysis. **Juan D. Jiménez:** Formal analysis, Data curation. **Chiyeop Kim:** Morphological analysis. **Tuan Van Nguyen:** Formal analysis, Resources, Data curation. **Kai Chen:** Resources, Data curation. **Periyayya Uthirakumar:** Software, Formal analysis. **Quyet Van Le:** Formal analysis, Resources, Data curation. **Sanjaya D. Senanayake:** Formal analysis, Data curation. **Hyun You Kim:** Visualization, Supervision, Project administration, Funding acquisition. **In-Hwan Lee:** Writing – review & editing, Visualization, Supervision, Project administration, Funding acquisition.

#### Declaration of Competing Interest

The authors declare that they have no known competing financial interests or personal relationships that could have appeared to influence the work reported in this paper.

#### Data Availability

The data that has been used is confidential.

#### Acknowledgments

This work was supported by the National Research Foundation of Korea (NRF) grant funded by the Korea government (MSIT) (2022R1A2C1010895, RS-2023-00208574) and by Samsung Research Funding & Incubation Center of Samsung Electronics under Project Number SRFC-TC2103-04. Computing time was provided by the National Institute of Supercomputing and Network/Korea Institute of Science and Technology Information (KSC-2021-CRE-0342, KSC-2022-CRE-0156). The work carried out at Brookhaven National Laboratory was supported by the US Department of Energy under contract no. DE-SC0012704. J.D.J acknowledges support from the Brookhaven National Laboratory Goldhaber Distinguished Fellowship.

#### Appendix A. Supplementary data

Supplementary material related to this article can be found in the online version.

#### Appendix A. Supporting information

Supplementary data associated with this article can be found in the online version at doi:10.1016/j.apcatb.2023.123452.

#### References

- [1] V.H. Hoa, D.T. Tran, S. Prabhakaran, D.H. Kim, N. Hameed, H. Wang, N.H. Kim, J. H. Lee, Ruthenium single atoms implanted continuous MoS<sub>2</sub>-Mo<sub>2</sub>C heterostructure for high-performance and stable water splitting, *Nano Energy* 88 (2021), 106277.
- [2] J. Lee, C. Yeon, J. Oh, G. Han, J. Do Yoo, H.J. Yun, C.-W. Lee, K.T. Lee, J. Bae, Highly active and stable catalyst with exsolved PtRu alloy nanoparticles for

- hydrogen production via commercial diesel reforming, *Appl. Catal. B: Environ.* 316 (2022), 121645.
- [3] H. Sun, L. Li, Y. Chen, H. Kim, X. Xu, D. Guan, Z. Hu, L. Zhang, Z. Shao, W. Jung, Boosting ethanol oxidation by NiOOH-CuO nano-heterostructure for energy-saving hydrogen production and biomass upgrading, *Appl. Catal. B: Environ.* 325 (2023), 122388.
  - [4] J. Mahmood, F. Li, S.-M. Jung, M.S. Okyay, I. Ahmad, S.-J. Kim, N. Park, H. Y. Jeong, J.-B. Baek, An efficient and pH-universal ruthenium-based catalyst for the hydrogen evolution reaction, *Nat. Nanotechnol.* 12 (2017) 441–446.
  - [5] X. Cheng, Y. Li, L. Zheng, Y. Yan, Y. Zhang, G. Chen, S. Sun, J. Zhang, Highly active, stable oxidized platinum clusters as electrocatalysts for the hydrogen evolution reaction, *Energy Environ. Sci.* 10 (2017) 2450–2458.
  - [6] G. Li, H. Jang, S. Liu, Z. Li, M.G. Kim, Q. Qin, X. Liu, J. Cho, The synergistic effect of Hf-O-Ru bonds and oxygen vacancies in Ru/HfO<sub>2</sub> for enhanced hydrogen evolution, *Nat. Commun.* 13 (2022) 1270.
  - [7] A. Kumar, V.Q. Bui, J. Lee, L. Wang, A.R. Jadhav, X. Liu, X. Shao, Y. Liu, J. Yu, Y. Hwang, H.T.D. Bui, S. Ajmal, M.G. Kim, S.-G. Kim, G.-S. Park, Y. Kawazoe, H. Lee, Moving beyond bimetallic-alloy to single-atom dimer atomic-interface for all-pH hydrogen evolution, *Nat. Commun.* 12 (2021) 6766.
  - [8] D. Wang, Q. Li, C. Han, Q. Lu, Z. Xing, X. Yang, Atomic and electronic modulation of self-supported nickel-vanadium layered double hydroxide to accelerate water splitting kinetics, *Nat. Commun.* 10 (2019) 3899.
  - [9] T. Liu, W. Gao, Q. Wang, M. Dou, Z. Zhang, F. Wang, Selective loading of atomic platinum on a RuCeO<sub>x</sub> support enables stable hydrogen evolution at high current densities, *Angew. Chem. Inter. Ed.* 59 (2020) 20423–20427.
  - [10] J. Dai, Y. Zhu, Y. Chen, X. Wen, M. Long, X. Wu, Z. Hu, D. Guan, X. Wang, C. Zhou, Q. Lin, Y. Sun, S.-C. Weng, H. Wang, W. Zhou, Z. Shao, Hydrogen spillover in complex oxide multifunctional sites improves acidic hydrogen evolution electrocatalysis, *Nat. Commun.* 13 (2022) 1189.
  - [11] Y. Han, H. Duan, W. Liu, C. Zhou, B. Wang, Q. Jiang, S. Feng, W. Yan, T. Tan, R. Zhang, Engineering the electronic structure of platinum single-atom sites via tailored porous carbon nanofibers for large-scale hydrogen production, *Appl. Catal. B: Environ.* 335 (2023), 122898.
  - [12] L. Wang, S. Chen, J. Hei, R. Gao, L. Liu, L. Su, G. Li, Z. Chen, Ultrafine, high-loading and oxygen-deficient cerium oxide embedded on mesoporous carbon nanosheets for superior lithium-oxygen batteries, *Nano Energy* 71 (2020), 104570.
  - [13] R. Schmitt, A. Nennung, O. Kraynis, R. Korobko, A.I. Frenkel, I. Lubomirsky, S. M. Haile, J.L.M. Rupp, A review of defect structure and chemistry in ceria and its solid solutions, *Chem. Soc. Rev.* 49 (2020) 554–592.
  - [14] D. Van Dao, T.T.D. Nguyen, H.-Y. Song, J.-K. Yang, T.-W. Kim, Y.-T. Yu, I.-H. Lee, Ionic liquid-assisted preparation of Ag-CeO<sub>2</sub> nanocomposites and their improved photocatalytic activity, *Mater. Des.* 159 (2018) 186–194.
  - [15] M. Molinari, S.C. Parker, D.C. Sayle, M.S. Islam, Water adsorption and its effect on the stability of low index stoichiometric and reduced surfaces of ceria, *J. Phys. Chem. C* 116 (2012) 7073–7082.
  - [16] D.V. Dao, T.T.D. Nguyen, P. Uthirakumar, Y.-H. Cho, G.-C. Kim, J.-K. Yang, D.-T. Tran, T.D. Le, H. Choi, H.Y. Kim, Y.-T. Yu, I.-H. Lee, Insightful understanding of hot-carrier generation and transfer in plasmonic Au@CeO<sub>2</sub> core-shell photocatalysts for light-driven hydrogen evolution improvement, *Appl. Catal. B: Environ.* 286 (2021), 119947.
  - [17] D. Van Dao, T.T.D. Nguyen, T.D. Le, S.-H. Kim, J.-K. Yang, I.-H. Lee, Y.-T. Yu, Plasmonically driven photocatalytic hydrogen evolution activity of a Pt-functionalized Au@CeO<sub>2</sub> core-shell catalyst under visible light, *J. Mater. Chem. A* 8 (2020) 7687–7694.
  - [18] M. Fronzi, S. Piccinin, B. Delley, E. Traversa, C. Stampfl, Water adsorption on the stoichiometric and reduced CeO<sub>2</sub>(111) surface: a first-principles investigation, *Phys. Chem. Chem. Phys.* 11 (2009) 9188–9199.
  - [19] M. Fronzi, A. Soon, B. Delley, E. Traversa, C. Stampfl, Stability and morphology of cerium oxide surfaces in an oxidizing environment: a first-principles investigation, *J. Chem. Phys.* 131 (2009), 104701.
  - [20] S. Gritschneider, Y. Iwasawa, M. Reichling, Strong adhesion of water to CeO<sub>2</sub>(111), *Nanotechnology* 18 (2007), 044025.
  - [21] S.D. Senanayake, D. Stacchiola, J. Evans, M. Estrella, L. Barrio, M. Pérez, J. Hrbek, J.A. Rodriguez, Probing the reaction intermediates for the water–gas shift over inverse CeO<sub>x</sub>/Au(111) catalysts, *J. Catal.* 271 (2010) 392–400.
  - [22] T. Miki, T. Ogawa, M. Haneda, N. Kakuta, A. Ueno, S. Tateishi, S. Matsuura, M. Sato, Enhanced oxygen storage capacity of cerium oxides in cerium dioxide/lanthanum sesquioxide/alumina containing precious metals, *J. Phys. Chem.* 94 (1990) 6464–6467.
  - [23] B.K. Cho, Chemical modification of catalyst support for enhancement of transient catalytic activity: nitric oxide reduction by carbon monoxide over rhodium, *J. Catal.* 131 (1991) 74–87.
  - [24] Y. Sun, T. Wu, Z. Bao, J. Moon, Z. Huang, Z. Chen, H. Chen, M. Li, Z. Yang, M. Chi, T.J. Toops, Z. Wu, D.-e. Jiang, J. Liu, S. Dai, Defect engineering of ceria nanocrystals for enhanced catalysis via a high-entropy oxide strategy, *ACS Cent. Sci.* 8 (2022) 1081–1090.
  - [25] Z. Xiao, C. Wu, L. Wang, J. Xu, Q. Zheng, L. Pan, J. Zou, X. Zhang, G. Li, Boosting hydrogen production from steam reforming of ethanol on nickel by lanthanum doped ceria, *Appl. Catal. B: Environ.* 286 (2021), 119884.
  - [26] D. Van Dao, H.D. Jung, T.T.D. Nguyen, S.-W. Ki, H. Son, K.-B. Bae, T.D. Le, Y.-H. Cho, J.-K. Yang, Y.-T. Yu, S. Back, I.-H. Lee, Defect-rich N-doped CeO<sub>2</sub> supported by N-doped graphene as a metal-free plasmonic hydrogen evolution photocatalyst, *J. Mater. Chem. A* 9 (2021) 10217–10230.
  - [27] J. Lim, J.-W. Jung, N.-Y. Kim, G.Y. Lee, H.J. Lee, Y. Lee, D.S. Choi, K.R. Yoon, Y.-H. Kim, I.-D. Kim, S.O. Kim, N<sub>2</sub>-dopant of graphene with electrochemically switchable bifunctional ORR/OER catalysis for Zn-air battery, *Energy Storage Mater.* 32 (2020) 517–524.
  - [28] Y.H. Kim, B.H. Park, Y.J. Choi, G.-W. Lee, H.-K. Kim, K.-B. Kim, Compact graphene powders with high volumetric capacitance: microspherical assembly of graphene via surface modification using cyanamide, *Energy Storage Mater.* 24 (2020) 351–361.
  - [29] S. Chen, J. Duan, J. Ran, M. Jaroniec, S.Z. Qiao, N-doped graphene film-confined nickel nanoparticles as a highly efficient three-dimensional oxygen evolution electrocatalyst, *Energy Environ. Sci.* 6 (2013) 3693–3699.
  - [30] D. Jang, Y. Lee, Y. Shin, S. Park, C. Jo, Y.-H. Kim, S. Park, Coordination structure of Jacobsen catalyst with N-modified graphene and their electrocatalytic properties for reducing oxygen molecules, *Appl. Catal. B: Environ.* 263 (2020), 118337.
  - [31] C. Liu, Y. Bai, Y. Zhao, H. Yao, H. Pang, MoS<sub>2</sub>/graphene composites: fabrication and electrochemical energy storage, *Energy Storage Mater.* 33 (2020) 470–502.
  - [32] K.M. Kamal, R. Narayan, N. Chandran, S. Popović, M.A. Nazrulla, J. Kovač, N. Vrtovec, M. Bele, N. Hodnik, M.M. Kržmanc, B. Likozar, Synergistic enhancement of photocatalytic CO<sub>2</sub> reduction by plasmonic Au nanoparticles on TiO<sub>2</sub> decorated N-graphene heterostructure catalyst for high selectivity methane production, *Appl. Catal. B: Environ.* 307 (2022), 121181.
  - [33] V. Dao, L.A. Cipriano, S.-W. Ki, S. Yadav, W. Wang, G. Di Liberto, K. Chen, H. Son, J.-K. Yang, G. Pacchioni, I.-H. Lee, 2D/2D Z-scheme-based α-Fe<sub>2</sub>O<sub>3</sub>@NGr heterojunction implanted with Pt single-atoms for remarkable photocatalytic hydrogen evolution, *Appl. Catal. B: Environ.* 330 (2023), 122586.
  - [34] D. Van Dao, L.A. Cipriano, G. Di Liberto, T.T.D. Nguyen, S.-W. Ki, H. Son, G.-C. Kim, K.H. Lee, J.-K. Yang, Y.-T. Yu, G. Pacchioni, I.-H. Lee, Plasmonic Au nanoclusters dispersed in nitrogen-doped graphene as a robust photocatalyst for light-to-hydrogen conversion, *J. Mater. Chem. A* 9 (2021) 22810–22819.
  - [35] X. Xiao, Y. Gao, L. Zhang, J. Zhang, Q. Zhang, Q. Li, H. Bao, J. Zhou, S. Miao, N. Chen, J. Wang, B. Jiang, C. Tian, H. Fu, A promoted charge separation/transfer system from Cu single atoms and C<sub>3</sub>N<sub>4</sub> layers for efficient photocatalysis, *Adv. Mater.* 32 (2020) 2003082.
  - [36] Z. Yu, Y. Li, A. Torres-Pinto, A.P. LaGrow, V.M. Diaconescu, L. Simonelli, M. J. Sampaio, O. Bondarchuk, I. Amorim, A. Araujo, A.M.T. Silva, C.G. Silva, J. L. Faria, L. Liu, Single-atom Ir and Ru anchored on graphitic carbon nitride for efficient and stable electrocatalytic/photocatalytic hydrogen evolution, *Appl. Catal. B: Environ.* 310 (2022), 121318.
  - [37] G. Di Liberto, L.A. Cipriano, G. Pacchioni, Role of dihydride and dihydrogen complexes in hydrogen evolution reaction on single-atom catalysts, *J. Am. Chem. Soc.* 143 (2021) 20431–20441.
  - [38] H. Jeong, O. Kwon, B.-S. Kim, J. Bae, S. Shin, H.-E. Kim, J. Kim, H. Lee, Highly durable metal ensemble catalysts with full dispersion for automotive applications beyond single-atom catalysts, *Nat. Catal.* 3 (2020) 368–375.
  - [39] W. Li, Y. Liu, M. Wu, X. Feng, S.A.T. Redfern, Y. Shang, X. Yong, T. Feng, K. Wu, Z. Liu, B. Li, Z. Chen, J.S. Tse, S. Lu, B. Yang, Carbon-quantum-dots-loaded ruthenium nanoparticles as an efficient electrocatalyst for hydrogen production in alkaline media, *Adv. Mater.* 30 (2018) 1800676.
  - [40] J. Xu, T. Liu, J. Li, B. Li, Y. Liu, B. Zhang, D. Xiong, I. Amorim, W. Li, L. Liu, Boosting the hydrogen evolution performance of ruthenium clusters through synergistic coupling with cobalt phosphide, *Energy Environ. Sci.* 11 (2018) 1819–1827.
  - [41] J. Zhang, Y. Gu, Y. Lu, C. Zhu, G. Liu, C. Wang, D. Sun, Y. Tang, H. Sun, Each performs its own functions: Nickel oxide supported ruthenium single-atoms and nanoclusters relay catalysis with multi-active sites for efficient alkaline hydrogen evolution reaction, *Appl. Catal. B: Environ.* 325 (2023), 122316.
  - [42] J. Zhang, G. Chen, Q. Liu, C. Fan, D. Sun, Y. Tang, H. Sun, X. Feng, Competitive adsorption: reducing the poisoning effect of adsorbed hydroxyl on Ru single-atom site with SnO<sub>2</sub> for efficient hydrogen evolution, *Angew. Chem.* 134 (2022), e202209486.
  - [43] L. Zhang, H. Jang, Y. Wang, Z. Li, W. Zhang, M.G. Kim, D. Yang, S. Liu, X. Liu, J. Cho, Exploring the dominant role of atomic- and nano-ruthenium as active sites for hydrogen evolution reaction in both acidic and alkaline media, *Adv. Sci.* 8 (2021) 2004516.
  - [44] Z. Li, Y. Pei, Q. Ju, B. Guo, Y. Hu, Q. Liu, Y. Zhu, J. Wang, A facile synthesis of Ru/N-C as an efficient and cost-effective electrocatalyst for hydrogen evolution, *N. J. Chem.* 44 (2020) 7962–7967.
  - [45] D.H. Kwon, M.S. Okyay, S.-J. Kim, J.-P. Jeon, H.-J. Noh, N. Park, J. Mahmood, J.-B. Baek, Ruthenium anchored on carbon nanotube electrocatalyst for hydrogen production with enhanced Faradaic efficiency, *Nat. Commun.* 11 (2020) 1278.
  - [46] J.P. Perdew, K. Burke, M. Ernzerhof, Generalized gradient approximation made simple, *Phys. Rev. Lett.* 77 (1996) 3865–3868.
  - [47] G. Kresse, D. Joubert, From ultrasoft pseudopotentials to the projector augmented-wave method, *Phys. Rev. B* 59 (1999) 1758–1775.
  - [48] J. Klimeš, A. Michaelides, Perspective: advances and challenges in treating van der Waals dispersion forces in density functional theory, *J. Chem. Phys.* 137 (2012).
  - [49] M. Yoo, Y.-S. Yu, H. Ha, S. Lee, J.-S. Choi, S. Oh, E. Kang, H. Choi, H. An, K.-S. Lee, J.Y. Park, R. Celestre, M.A. Marcus, K. Nowrouzi, D. Taube, D.A. Shapiro, W. Jung, C. Kim, H.Y. Kim, A tailored oxide interface creates dense Pt single-atom catalysts with high catalytic activity, *Energy Environ. Sci.* 13 (2020) 1231–1239.
  - [50] H.Y. Kim, M.S. Hybertsen, P. Liu, Controlled growth of ceria nanoarrays on anatase titania powder: a bottom-up physical picture, *Nano Lett.* 17 (2017) 348–354.
  - [51] B. Liu, Y.-F. Zhao, H.-Q. Peng, Z.-Y. Zhang, C.-K. Sit, M.-F. Yuen, T.-R. Zhang, C.-S. Lee, W.-J. Zhang, Nickel-cobalt diselenide 3D mesoporous nanosheet networks supported on Ni foam: an all-pH highly efficient integrated electrocatalyst for hydrogen evolution, *Adv. Mater.* 29 (2017) 1606521.



- [52] B. Xu, Q. Zhang, S. Yuan, M. Zhang, T. Ohno, Synthesis and photocatalytic performance of yttrium-doped CeO<sub>2</sub> with a porous broom-like hierarchical structure, *Appl. Catal. B: Environ.* 183 (2016) 361–370.
- [53] S.E. Sivan, K.H. Kang, S.J. Han, O. Francis Ngome Okello, S.-Y. Choi, V. Sudheeshkumar, R.W.J. Scott, H.-J. Chae, S. Park, U.H. Lee, Facile MOF-derived one-pot synthetic approach toward Ru single atoms, nanoclusters, and nanoparticles dispersed on CeO<sub>2</sub> supports for enhanced ammonia synthesis, *J. Catal.* 408 (2022) 316–328.
- [54] L. Nie, D. Mei, H. Xiong, B. Peng, Z. Ren, X.L.P. Hernandez, A. DeLaRiva, M. Wang, M.H. Engelhard, L. Kovarik, A.K. Datye, Y. Wang, Activation of surface lattice oxygen in single-atom Pt/CeO<sub>2</sub> for low-temperature CO oxidation, *Science* 358 (2017) 1419–1423.
- [55] H. Fan, F. Qin, Q. Yuan, Z. Sun, H. Gu, W. Xu, H. Tang, S. Liu, Y. Wang, W. Chen, J. Li, H. Zhai, Improving the selectivity of hydrogenation and hydrodeoxygenation for vanillin by using vacancy-coupled Ru–N<sub>3</sub> single atoms immobilized on defective boron nitride, *J. Mater. Chem. A* 11 (2023) 17560–17569.
- [56] Z. Liu, H. Li, X. Gao, X. Guo, S. Wang, Y. Fang, G. Song, Rational highly dispersed ruthenium for reductive catalytic fractionation of lignocellulose, *Nat. Commun.* 13 (2022) 4716.
- [57] C. Zhang, J. Sha, H. Fei, M. Liu, S. Yazdi, J. Zhang, Q. Zhong, X. Zou, N. Zhao, H. Yu, Z. Jiang, E. Ringe, B.I. Yakobson, J. Dong, D. Chen, J.M. Tour, Single-atomic ruthenium catalytic sites on nitrogen-doped graphene for oxygen reduction reaction in acidic medium, *ACS Nano* 11 (2017) 6930–6941.
- [58] H. Qi, J. Yang, F. Liu, L. Zhang, J. Yang, X. Liu, L. Li, Y. Su, Y. Liu, R. Hao, A. Wang, T. Zhang, Highly selective and robust single-atom catalyst Ru<sub>1</sub>/NC for reductive amination of aldehydes/ketones, *Nat. Commun.* 12 (2021) 3295.
- [59] M. Michalska, K. Lemański, A. Sikora, Spectroscopic and structural properties of CeO<sub>2</sub> nanocrystals doped with La<sup>3+</sup>, Nd<sup>3+</sup> and modified on their surface with Ag nanoparticles, *Heliyon* 7 (2021), e06958.
- [60] Y. Lee, G. He, A.J. Akey, R. Si, M. Flytzani-Stephanopoulos, I.P. Herman, Raman analysis of mode softening in nanoparticle CeO<sub>2–δ</sub> and Au–CeO<sub>2–δ</sub> during CO oxidation, *J. Am. Chem. Soc.* 133 (2011) 12952–12955.
- [61] P.G. Callahan, B.J. Jaques, B.M. Marx, A.S. Hamdy, D.D. Osterberg, D.P. Butt, Synthesis of dysprosium and cerium nitrides by a mechanically induced gas–solid reaction, *J. Nucl. Mater.* 392 (2009) 121–124.
- [62] J.R. McBride, K.C. Hass, B.D. Poindexter, W.H. Weber, Raman and x-ray studies of Ce<sub>1–x</sub>RE<sub>x</sub>O<sub>2–y</sub>, where RE=La, Pr, Nd, Eu, Gd, and Tb, *J. Appl. Phys.* 76 (1994) 2435–2441.
- [63] S.C. Shrivhate, A.K. Yadav, S.A. Acharya, Extended x-ray absorption fine structure spectroscopy and x-ray absorption near edge spectroscopy study of aliovalent doped ceria to correlate local structural changes with oxygen vacancies clustering, *Appl. Phys. Lett.* 108 (2016).
- [64] M. Ismael, Y. Wu, A facile synthesis method for fabrication of LaFeO<sub>3</sub>/g-C<sub>3</sub>N<sub>4</sub> nanocomposite as efficient visible-light-driven photocatalyst for photodegradation of RhB and 4-CP, *N. J. Chem.* 43 (2019) 13783–13793.
- [65] C. Fan, C. Chen, J. Wang, X. Fu, Z. Ren, G. Qian, Z. Wang, Black hydroxylated titanium dioxide prepared via ultrasonication with enhanced photocatalytic activity, *Sci. Rep.* 5 (2015) 11712.
- [66] D. Van Dao, H. Choi, T.T.D. Nguyen, S.-W. Ki, G.-C. Kim, H. Son, J.-K. Yang, Y.-T. Yu, H.Y. Kim, I.-H. Lee, Light-to-hydrogen improvement based on three-factored Au@CeO<sub>2</sub>/Gr hierarchical photocatalysts, *ACS Nano* 16 (2022) 7848–7860.
- [67] C.H. Choi, M.W. Chung, H.C. Kwon, J.H. Chung, S.I. Woo, Nitrogen-doped graphene/carbon nanotube self-assembly for efficient oxygen reduction reaction in acid media, *Appl. Catal. B: Environ.* 144 (2014) 760–766.
- [68] P.K.L. Tran, D.T. Tran, M. Austeria P, D.H. Kim, N.H. Kim, J.H. Lee, Intermolecular metallic single-site complexes dispersed on Mo<sub>2</sub>TiC<sub>2</sub>T<sub>x</sub>/MoS<sub>2</sub> heterostructure induce boosted solar-driven water splitting, *Adv. Energy Mater.* 13 (2023) 2203844.
- [69] B.E. Conway, B.V. Tilak, Interfacial processes involving electrocatalytic evolution and oxidation of H<sub>2</sub>, and the role of chemisorbed H, *Electrochim. Acta* 47 (2002) 3571–3594.
- [70] G. Zhao, K. Rui, S.X. Dou, W. Sun, Heterostructures for electrochemical hydrogen evolution reaction: a review, *Adv. Funct. Mater.* 28 (2018) 1803291.
- [71] C. Li, H. Jang, M.G. Kim, L. Hou, X. Liu, J. Cho, Ru-incorporated oxygen-vacancy-enriched MoO<sub>2</sub> electrocatalysts for hydrogen evolution reaction, *Appl. Catal. B: Environ.* 307 (2022), 121204.
- [72] D.R. Mullins, P.M. Albrecht, T.-L. Chen, F.C. Calaza, M.D. Biegalski, H.M. Christen, S.H. Overbury, Water dissociation on CeO<sub>2</sub>(100) and CeO<sub>2</sub>(111) thin films, *J. Phys. Chem. C* 116 (2012) 19419–19428.